Comparison of Physical and Chemical Vapor Deposition for Magnesium Intercalation Underneath Epitaxial Graphene

Patrick A. Rondomanski[1], Anushka Bansal[1], Chengye Dong[1], Ke Wang[3], Jennifer L. Gray[3], Jeffrey R. Shallenberger[3], Joshua A. Robinson[1,4], Qi Li[1,2,3], Joan M. Redwing[1,3,4,a]

[1]Department of Materials Science & Engineering, The Pennsylvania State University, University Park, PA USA

[2]Department of Physics, The Pennsylvania State University, University Park, PA USA

[3]Materials Research Institute, The Pennsylvania State University, University Park, PA USA

[4]2D Crystal Consortium Materials Innovation Platform, Materials Research Institute, The Pennsylvania State University, University Park, PA USA

[a]Corresponding Author: Joan Redwing, jmr31@psu.edu

Key words

A3. Metalorganic chemical vapor deposition; A3. Physical vapor deposition processes; A1. Doping; A1. Intercalation; B1. Epitaxial Graphene

Abstract

Intercalation of Mg into epitaxial graphene was investigated using chemical vapor deposition (CVD) and physical vapor deposition (PVD) for the formation of n-type doped graphene. Scanning electron microscopy and atomic force microscopy indicate PVD has significantly greater metal deposition and surface roughness compared to the CVD process.

Findings from x-ray photoelectron spectroscopy infer the formation of Mg intercalated quasi-freestanding epitaxial graphene indicated by shifting of the SiC peak in C 1s spectra. This is substantiated by visual evidence from scanning tunneling electron microscopy of up to three layers of Mg residing underneath EG. Furthermore, an invariant 2D peak position in Raman spectra taken over a 7-day period in ambient conditions support arguments of the stability of electron doped Mg-intercalated epitaxial graphene. CVD offers a cleaner and smoother surface compared to PVD due to improved control over when the substrate is subjected to Mg exposure, but PVD allows for greater Mg concentrations per minute that may increase the amount of intercalated metal.

1.0 Introduction

The physical and electrical properties of graphene such as high mechanical strength and low sheet resistance, are well known and have made it an appealing material for the fabrication of transparent and ultra-thin devices, such as biosensors, photodetectors, and FETs[1–8]. Utilization of graphene as interconnects and electrodes is desirable for these types of devices, but some applications, such as solar cells, require the graphene to be heavily n-type doped to perform suitably in these roles[9].

There are several approaches to tune graphene's electrical properties, such as gating[10–12], intercalation[13–15], and chemical substitution[16]. Of these, chemical doping via intercalation offers the opportunity for highly-doped graphene that can be readily integrated into a broad range of device designs. In order to achieve broad applicability, it is imperative for the chemical doping to yield a graphene layer that is not only highly doped but also resistant to environmental factors. However, synthesizing stable n-doped graphene has proven to be challenging, primarily stemming from the inherently reactive and air-sensitive nature of n-type dopants, typically metals.

Intercalation instability may inhibit the physical and electronic decoupling of graphene from the substrate if the metals deintercalated and hinder electron donation due to metal oxidation. While there have been a handful of n-type intercalants demonstrated, such as Li[17,18] and Ca[19,20], few successful demonstrations of air-stable, n-doped single-layer graphene exist, such as $CsCO_3$[21] and ZnO[22] doping. It is worth noting, however, that these dopants do not significantly surpass the natural electron doping levels observed in monolayer graphene epitaxially grown on silicon carbide (EG)[23], underscoring the need for robust and highly n-doped graphene. .

Magnesium (Mg) has been shown to intercalate into EG and produce Mg intercalated quasi-freestanding epitaxial graphene (Mg-QFEG), an n-type doped graphene with carrier densities reported up to $n = 2.1\times10^{14}$ cm^{-2} [19,24]. Additionally, the Mg-QFEG was reported to remain air stable for at least a few hours. Mg intercalation has also been demonstrated using CVD grown graphene on Ni (111)[25]. Thus, Mg is a potential candidate for the modification of graphene for device applications that require n-type doping.

Thus far, Mg intercalation into EG has only been demonstrated in ultra-high vacuum using molecular beam epitaxy[19]. Scalable processes such as chemical vapor deposition (CVD) and physical vapor deposition (PVD) which can be carried out at low to moderate pressures are desired to integrate Mg-QFEG into commercially scalable device fabrication. PVD has advantages of simple equipment, such as a tube furnace, and a high partial pressure in the vapor phase which is beneficial to drive intercalation. However, it is more challenging to control the partial pressure which can lead to metal accumulation on the substrate surface and oxygen impurities from native oxides associated with the source materials. This technique is largely used in confinement heteroepitaxy (CHet) studies with success in producing intercalated Ag, In, Ga, Sn, and various metal oxides[26–29]. Benefits of the CVD process include operation at moderate pressures and precise

control over exposure time and partial pressure of precursors to reduce metal agglomeration on surfaces. Success using metalorganic sources has been observed using trimethylgallium (TMGa) for Ga interclation[30,31]. The caveat is that metalorganic sources may impose impurities of C or O from the decomposition of precursors ligands. Hence, depending on the manufacturing situation, one technique may be more applicable than the other. Therefore, CVD and PVD should be explored to determine their viability to expand the applications of magnesium intercalation on a larger scale.

In this study, we demonstrate Mg intercalation into EG using both PVD and CVD at atmospheric pressure and 300 Torr, respectively. The intercalated samples prepared by PVD and CVD were characterized using x-ray photoelectron spectroscopy (XPS), Raman spectroscopy, atomic force microscopy (AFM), field-emission scanning electron microscopy (FESEM), and scanning tunneling electron microscopy with electron dispersion spectroscopy (STEM-EDS). Characteristic indications of intercalation were observed in changes to the binding energy of the C 1s spectrum in XPS. This indirect method is further supported with visual evidence of the sample cross-section using STEM-EDS which revealed decoupled graphene above a layer(s) of Mg-containing material. Lastly, consistent with prior approaches, the stability of the n-type doping in air was assessed via Raman measurements carried out for up to 7 days. Thus, air-stable, n-doped graphene was achieved for implementation into large-scale EG device applications.

2.0 Experimental

Epitaxial Graphene Synthesis

Epitaxially grown graphene on semi-insulating 6H-SiC (EG) was produced using standard synthesis techniques[32,33]. EG is grown via sublimating Si atoms from the Si face of 6H semi-

insulating silicon carbide (II-VI Inc.). First, SiC substrates are etched at 1500 ℃ with 10% H_2/Ar mixture for 30 min. Then they are heated at 1800 ℃ in pure argon for 20 min to grow monolayer EG (MLEG). Buffer layer graphene on SiC (BLEG) is obtained by peeling off the quasi-free standing layer of sp^2 graphene from MLEG samples to leave only the sp^3 hybridized graphene layer that was initially formed in MLEG synthesis. 270 nm thick Ni, E-beam deposited on MLEG with a rate of 5 Å/s, acts as a stress layer. Then double-side thermal release tape is used to peel off the Ni and graphene layer together and leave the buffer layer on SiC substrates. Hydrogenated BLEG (H-1L-QFEG) is synthesized via annealing BLEG at 700 ℃ in pure hydrogen for 30 min.

Graphene thicknesses utilized ranged from BLEG to MLEG, such that magnesium intercalated quasi-free standing monolayer graphene (Mg-1L-QFEG) or magnesium intercalated quasi-free standing bilayer graphene (Mg-2L-QFEG) would be produced, respectively. Due to EG substrate availability, BLEG and MLEG were used for CVD and PVD experiments, respectively. Additionally, H-1L-QFEG was examined to determine if there is evidence of Mg intercalation due to coexistence with or replacement of the H.

Metal Intercalation

PVD intercalation into MLEG was initially carried out using a horizontal hot-walled tube furnace. A custom stainless steel foil boat was constructed to allow a sample-holding lid to cap the boat, such that a single Mg pellet or shaving would be placed below an upside down MLEG substrate for Mg exposure [Fig. 1a]. Mg sources were cleaned with a 1:10 HCl:DI water solution to remove surface contaminants and reduce the amount of surface oxide. An inert environment was established by flowing 50 sccm of high-purity Ar through the furnace. Successful intercalation was achieved with a growth temperature of 500 °C for 35 min at atmospheric pressure. The sample was cooled to room temperature with a rate of ~10 °C/min. A rapid cooldown was observed to

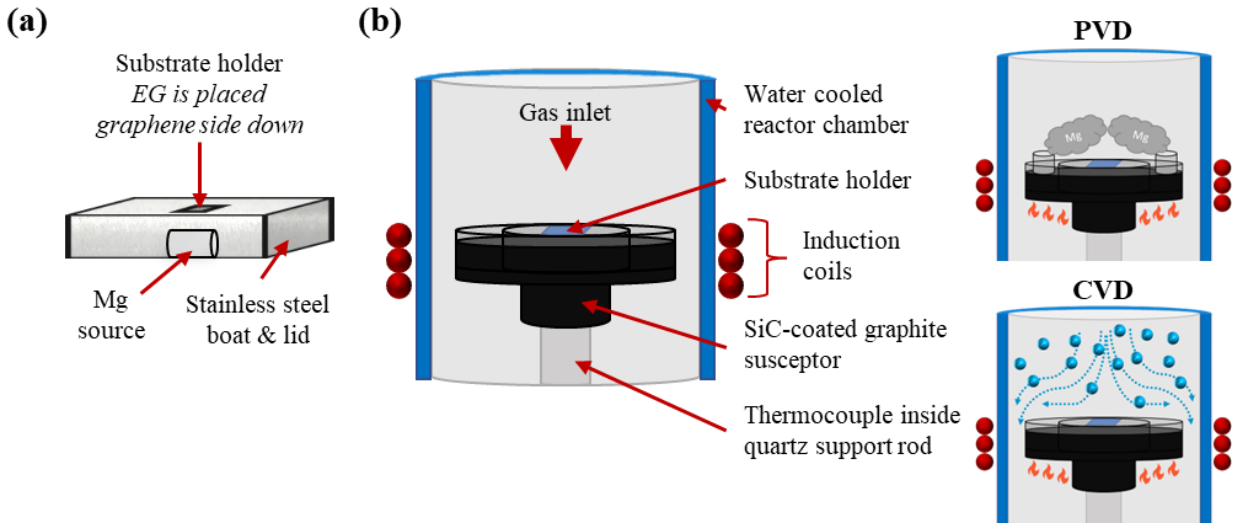

FIG. 1. (a) Schematic of the boat design employed for PVD synthesis of Mg-2L-QFEG in a hot-walled tube furnace. (b) Vapor deposition system schematic of the cold-walled reactor used for synthesis of Mg-1L-QFEG via PVD and CVD methods.

impede successful intercalation. Additional PVD intercalation was carried out using BLEG in a cold-wall hybrid physical-chemical vapor deposition (HPCVD) reactor [Fig. 1b]. The HPCVD reactor consists of an inductively heated SiC-coated graphite susceptor, designed to retain ½ inch metal pellets around the substrate, supported by a quartz rod, harboring a thermocouple, inside a water-cooled vertical quartz tube chamber. Two Mg pellets were placed on the inductively heated susceptor, located 180° from each other, for the Mg source. The process conditions in the HPCVD reactor were similar to the tube furnace. Growth temperature was 500 °C for 15 min at 700 Torr with 400 sccm carrier gas flow of high purity Ar and the sample was cooled to room temperature at 10 °C/min. Growth time was reduced to compensate for greater Mg sublimation from lower pressure and the increased Mg flux due to a larger carrier gas flow and two metal sources. Note that the use of different graphene layer thicknesses for PVD work was due to substrate availability.

The HPCVD system was also used to carry out CVD intercalation of Mg into BLEG [Fig. 1b] using either bis(methylcyclopentadienyl)magnesium ($(MeCp)_2Mg$) or bis(cyclopentadienyl)magnesium (Cp_2Mg) as the magnesium source. $(MeCp)_2Mg$ allows for

greater Mg concentrations compared to Cp_2Mg under identical bubbler conditions , as has been noted before with use in doping GaN[34,35]. Precursor flow rates at a bubbler temperature and pressure of 45 °C and 400 Torr, respectively and 80 sccm of Ar carrier gas were estimated to be approximately 0.0668 sccm for Cp_2Mg and 0.1537 sccm for $(MeCp)_2Mg$. To increase the flux of the Mg precursor from the bubbler, it was necessary to use a bubbler pressure below atmospheric pressure which subsequently restricted the reactor pressure to below 400 Torr. Effective conditions utilized 4-6 min of precursor exposure time at a temperature of 800 °C under 300 Torr with 400 sccm carrier gas flow of high purity Ar.

Characterization Techniques

Raman spectroscopy was performed with a WITec A300 (Ulm, DE) using a 532 nm laser through a 100x objective lens at 10 mW power with 5 s acquisition time for 6 accumulations. AFM was executed using a Bruker Icon (Billerica, MA, USA). FESEM was done using a Gemini 500 (Zeiss, Oberkochen, DE). High angle annular dark field STEM with EDS was conducted with an FEI Titan3 G2 (Hillsboro, OR, US) at 200 kV on samples prepared using a focused ion beam. The surface of samples was first coated with a protective carbon layer before milling.

XPS was carried out using a Physical Electronics VersaProbe III (Chanhassen, MN, USA) equipped with a monochromatic Al kα x-ray source (hν = 1,486.6 eV) and a concentric hemispherical analyzer. All spectra, except for buffer layer graphene reference, were calibrated to the carbon sp^2 peak in the carbon 1s spectra at 284.5 eV. Buffer layer graphene was calibrated to the bulk SiC peak at 283.7 eV. Standard measurements were made at an angle of 45° with respect to the sample surface plane and an analysis size of ~200 μm in diameter. Angle resolved measurements were taken at 30° and 80°. Quantification was done using instrumental relative

sensitivity factors that account for the x-ray cross section and inelastic mean free path of the electrons.

3.0 Results & Discussion

The surface morphology of the epitaxial graphene after Mg intercalation via PVD and CVD under optimized conditions is shown in Fig. 2. FESEM micrographs of the surfaces of PVD Mg-2L-QFEG and CVD Mg-1L-QFEG samples are shown in Fig. 2a. The PVD surface consists of wrinkles and step edges that are decorated with Mg crystallites (bright contrast) that range up to hundreds of nanometers in size. Higher magnification image (inset) also reveals the presence of nanoparticles in the regions between the wrinkles. In contrast, the CVD surface is relatively smooth without evidence of wrinkles and large particles. However, high magnification imaging

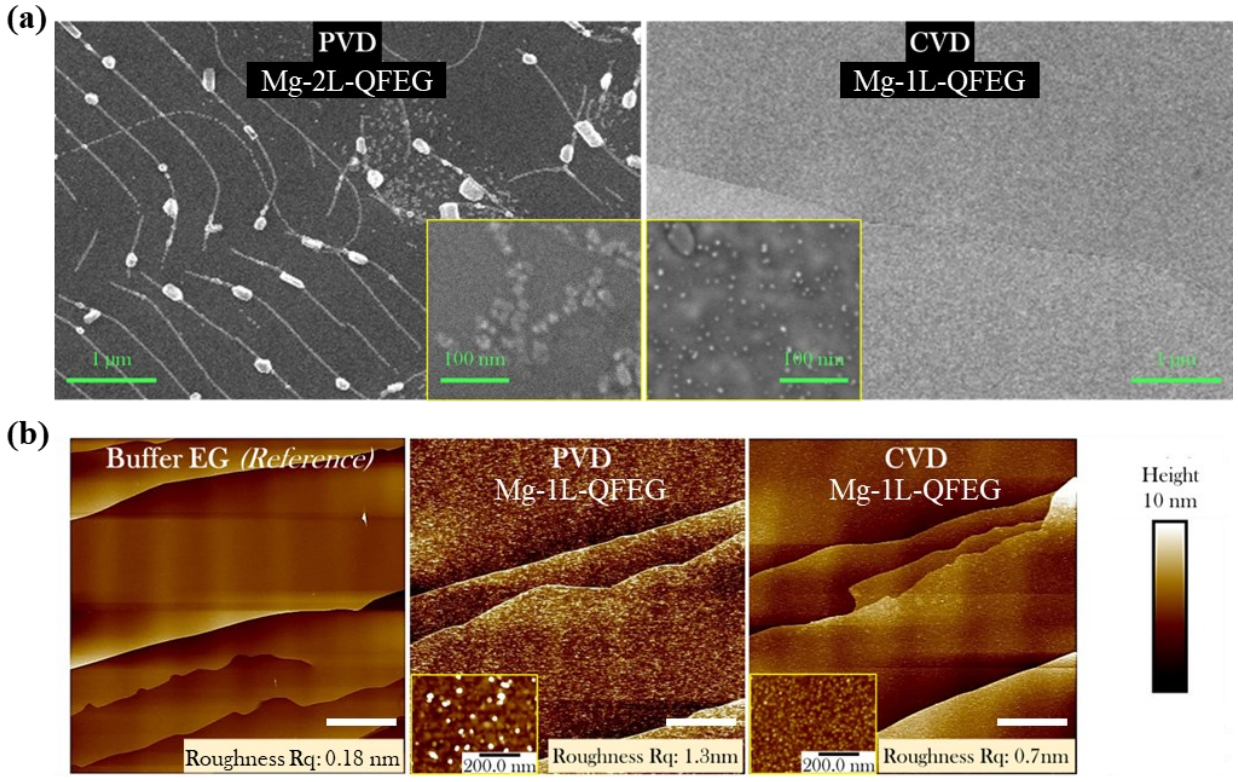

FIG. 2. FESEM (a) and AFM (b) micrographs display the notable difference in surface roughness and Mg residue from the PVD and CVD methods. The excessive Mg from PVD would be more problematic for devices that require a clean graphene surface. This is due to the lack of control in the PVD process compared to CVD, where the Mg flow can be started and stopped on command. Unmarked scale bars in (b) are 2 μm.

(inset) reveals the presence of nanoscale particles similar to the PVD sample but smaller at ≤10 nm in size. In Fig. 2b, AFM analysis of Mg-1L-QFEG reveals the Rq surface roughness of the CVD samples as 0.7 nm, an approximate 0.5 nm increase in from the bare BLEG substrate (0.18 nm). The Rq surface roughness of the PVD samples is ~1.3 nm. Zooming in on the steps (insets) indicates the same results as FESEM, the presence of nanoparticles that coat the EG surface and PVD consisting of slightly larger particulates.

There are two prominent factors for the variance observed between the two techniques. First, in the PVD approach, the Mg continues to evaporate as the cooldown process begins whereas in CVD the Mg flow can be halted. One of the notable differences between PVD and CVD processes is the extent of Mg deposition on the substrate. Both processes will result in surface residue of Mg, even under optimized conditions. However, CVD allows for precise control over the duration and quantity of precursor exposure in the reactor, whereas the physical source's sublimation rate in PVD is limited by the chamber configuration from the reactor's temperature and pressure for the entirety of the growth process.

Second, the growth parameters of CVD are considerably different than that of PVD. In PVD, surface deposition of Mg increased dramatically with temperature due to increased vaporization from the pellet sources, consequently, lower temperatures still allowed for suitable amounts of Mg vaporization at temperatures below its melting point of 650 °C. The amount of Mg evaporated at 500 °C for 35 min was not accurately measurable but was likely on the order of micrograms. Conversely for CVD, higher temperatures up to 800 °C were found to be necessary for Mg intercalation, likely due to greater thermal energy to decompose the ligands from the metalorganic precursors and promote diffusion of Mg through the graphene. Moreover, higher temperatures are known to promote defects in graphene, even in an inert environment, that could

serve to improve intercalation as well[28,30,36–38]. The lower pressure combined with higher temperature for CVD also allows for greater sublimation of residual Mg off the graphene surface during the cooldown. The differences between the PVD and CVD sources and delivery geometries are the predominant reasons for the longer PVD intercalation time relative to that of CVD. Therefore, with limited control of Mg sublimation, lower temperature, higher pressure, and shortened cooldown duration, the PVD approach understandably resulted in a more heavily structured surface.

XPS is a prominently used nondestructive technique to evaluate metal intercalated EG. Basic spectra of the C 1s for both BLEG and MLEG are displayed in Fig. 3(a) (top) and contain peaks corresponding to the SiC substrate (SiC) and peaks associated with the graphene including the reconstructed graphene buffer layer of hybridized sp^3 carbon (S1 and S2), graphene as sp^2 carbon (G), and oxygen functionalized carbon (O^1)[39]. Fitting the substrate peaks places the SiC peaks at 283.7 eV, in good agreement with other sources[19,39]. As would be expected, the BLEG as-grown lacks the G peak present in MLEG due to it nominally containing no sp^2 carbon. The S1/S2 contribution is much smaller in MLEG due to the dominance of sp^2 carbon. The oxygen presence in BLEG is due to an increased density of carbon atoms with dangling bonds that oxidize during handling and storage, as noted in other works[30].

After the EG substrates were exposed to Mg via CVD, Fig. 3(a) (lower left), or PVD, Fig. 3(a) (lower right), there are noticeable changes to the spectra. Firstly, in the CVD sample the S1, 285.0 ± 0.2 eV, and S2, 285.5 ± 0.2 eV, peaks are replaced with only a G peak at 284.5 eV. This implies that the partially bound graphene buffer layer has decoupled from the SiC substrate and is now a quasi-free standing graphene layer. The continued presence of the S1/S2 peaks for the PVD sample, used to better fit the Mg-2L-QFEG spectra, implies that there may be some region of

graphene that is not intercalated in the sample. Secondly, discernible for both PVD and CVD samples is peak shift of the SiC, labelled SiC'. A commonly sought after indication of an intercalated metal is a shifting of the SiC peak toward a lower energy in the C 1s spectrum due to a modification in charge transfer between graphene and SiC[28,40,41]. PVD produces a slightly lower energy SiC', 282.5 eV, than CVD does, 282.9 eV, by ~0.4 eV. Often, a smaller energy shift of the SiC is indicative of lesser intercalation. This could be the case because PVD does deposit more Mg than CVD, as already discussed. Therefore, it would stand to reason that PVD may produce greater coverage of intercalated material. This effect has also been seen in samples that had longer metalorganic Mg exposure time.

In addition to the expected SiC', there is a second shift to lower energy SiC peak, SiC", seen for the PVD sample. An explanation from this may come from a similar observation seen for H-1L-QFEG that was exposed to Mg and left in ambient conditions [Fig. 3b]. This sample was known to contain excessive wrinkles and tears that exposed the SiC substrate due to etching of the buffer layer graphene during the hydrogenation process. These are similar to defects that the PVD sample contained prior to growth and were evident in the SEM analysis seen in Fig. 2(a). In Fig. 3(b) we can see that over a period of 7 days of ambient air exposure, the SiC" appears and begins to dominate over the SiC'. An additional oxygen functionalized carbon peak, O^2, also appears and is potentially the result of additional defects in the graphene arising from intercalation that result in extra dangling bonds for oxidation. Thus, the SiC" peak present in both the PVD sample and Mg-exposed H-1L-QFEG may be the result of MgO forming on exposed SiC or graphene wrinkles.

Angle-resolved XPS (AR-XPS) can be used to obtain depth-resolved information about layer stacking order from the concentration profile of elements in a sample. Fig. 3(c) (left) is a depth-resolved profile of a CVD Mg-1L-QFEG sample which indicates graphene as the uppermost

material, followed by the maximum of the Mg concentration that sits above the C and Si components of the SiC substrate. In this profile, the greatest oxygen content is located above the Mg and close to the graphene. This could be explained by a thin layer of oxidized graphene or MgO on top of the graphene that would put the averages on similar levels. The PVD Mg-1L-QFEG profile, Fig. 3(c) (right), exhibits similar results where graphene is the material nearest the surface, followed by the predominant Mg concentration that is located above the C and Si components of the SiC substrate. However, the maximum oxygen level is located beneath the Mg in this case. One explanation for this could be a greater amount of surface Mg in the PVD sample that would shift the maximum in the Mg concentration closer to the

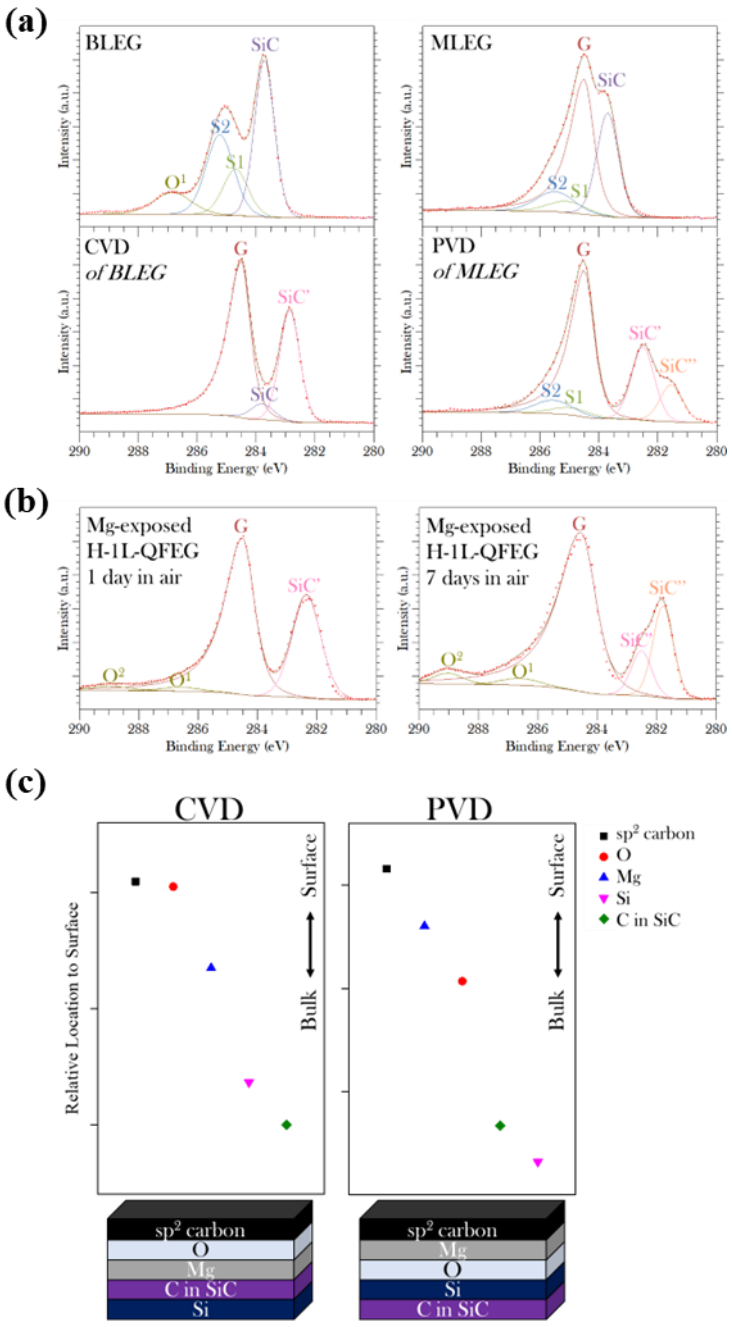

FIG. 3. (a) XPS C 1s results before and after Mg intercalation of buffer and monolayer EG. The S1/S2 peaks represent the buffer layer whereas G is a full graphene layer. ~1 eV shifts in the SiC peak, SiC', are expected indications of intercalation. The second shifted SiC peak, SiC", is potentially due to MgO formation on exposed SiC. (b) This comes from similar observations of Mg-exposed H-1L-QFEG exposed to air, where SiC is knowingly exposed. O^1/O^2 are expected to be C-O-C and C=O-C formed from damaged graphene when left in air. (c) AR-XPS offers a second technique to infer that the average Mg concentration is below graphene in Mg-1L-QFEG.

surface. Another explanation could be the introduction of oxygen impurities from the native MgO that coats the Mg pellets, whereas the CVD bubbler source is air-tight. Further work with a greater sampling would be needed to add significance to this observation.

While not presented in this work, Mg 2p, O 1s, and Si 2p spectra were collected for all samples presented in Fig. 3. These data were omitted due to a lack of resolution to adequately deconvolute the spectra and identify their chemical origin. Consequently, XPS was deemed unsuitable to determine the extent of Mg intercalation and the location of any MgO present, relative to the graphene, as the XPS signal from Mg could be coming from the surface or the graphene/SiC interface. The only spectra with significance were deviations of the Si 2p that matched the shifts toward lower energy of the C 1s SiC peak to the SiC' and SiC" peaks. As a result of this observation, the anomalous peak is referenced as also arising from silicon carbide. Resolution of the Si 2p was not capable of distinguishing any Mg-Si type bonds as observed in other works[19].

Successful intercalation of Mg into MLEG via PVD to create Mg-2L-QFEG was demonstrated using cross-sectional STEM-EDS [Fig. 4]. In the STEM micrograph, the bilayer graphene is decoupled from the SiC substrate via an interlayer that contains Mg as demonstrated by EDS. A line of Mg measured by EDS between the graphene and SiC interfaces has a corresponding line of increased O. Due to its high reactivity, it's expected the Mg will oxidize during the processing of the TEM sample from air exposure. In addition, oxidation of the Mg may result in amorphous material which is consistent with the structure of the interlayer in the STEM image. While this technique is a viable method of determining the presence of Mg below graphene, it does not allow us to determine if the graphene inhibits oxidation of the underlying metal. Additionally, the oxidation during processing and small atomic size of Mg makes it difficult to determine the number of layers of intercalated Mg and its structure.

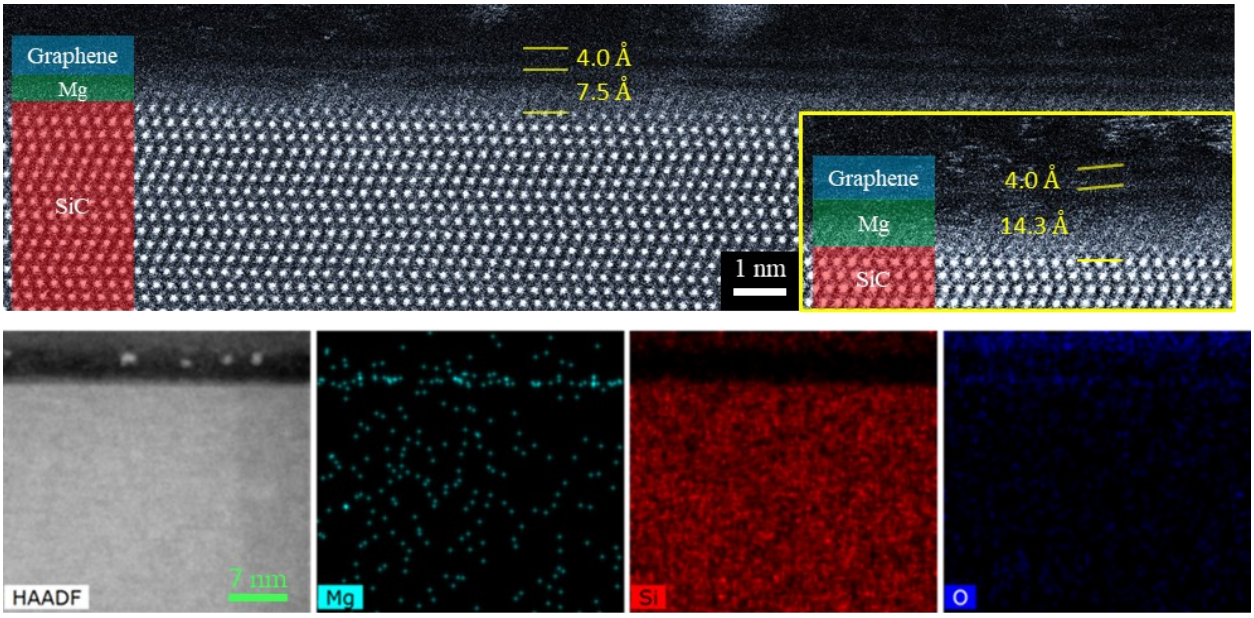

FIG. 4. STEM-EDS of Mg-2L-QFEG produced using PVD. Inset is a region of greater Mg intercalation of the same sample, emphasizing the nonuniformity of intercalation. Diverse distances between the SiC and graphene suggest varied thicknesses of confined Mg.

Estimated measurements of the lattice spacing offer insight to the amount of Mg that may be confined beneath the graphene. As a reference, the spacing of the graphene layers in Fig. 4 measures approximately 4.0 Å (expected 3.3 Å). The average distance between the graphene and SiC is approximately 7.5 Å. While this spacing is more than adequate for a layer of Mg (metallic Mg has an expected lattice constant of 5.1 Å), it is difficult to precisely determine how much Mg may be present due to a lack of knowledge of the interfacial bonding between the metal and substrate. Prior XPS characterization of MBE grown Mg intercalated EG suggested that the Mg-SiC interfacial layer may contain a magnesium silicide-like compound due to binding between the Mg and Si-terminated substrate[19]. Higher resolution imaging would be required to properly determine any Mg:Si bond stoichiometries and the crystal structure at this substrate/metal interface for these materials. However, knowledge from known bulk materials can be used to speculate on this material. Using Mg_2Si ($Fm\bar{3}m$) as a reference[42], the spacing between Mg-Si atoms is roughly 2.7 Å. Therefore, a distance similar to the measured 7.5 Å spacing between graphene and SiC in

Fig. 4 can be obtained by summing a covalently bound Mg-Si, 2.7 Å, and van der Waals bound Mg-graphene, 4.0 Å. This estimation uses the van der Waals spacing measured between the graphene layers in Fig. 4, the estimated covalent bond spacing of bulk Mg_2Si, and would have an error of $\pm$ 0.7 Å taken from the measured graphene spacing in Fig. 4. Thus, one could reasonably speculate to there being a single layer of Mg intercalated underneath the graphene in this region of the sample presented in Fig. 4.

A STEM image from another region of the sample included in the inset of Fig. 4, shows a significantly larger gap between graphene and SiC. In this region, there appears to be an approximately 14.3 Å spacing between substrate and graphene. This could realistically accommodate multiple layers of close-packed Mg. Therefore, it is evident that an inhomogeneous number of layers of Mg may be intercalated via PVD. This nonuniformity in thickness may coincide with the slightly larger shift seen in the XPS of the PVD C 1s SiC' peak to suggest a greater extent of Mg intercalation.

STEM-EDS was performed on Mg-1L-QFEG synthesized using CVD as well. Spacing of the graphene from the substrate did suggest the buffer layer was decoupled across most of the micrographs collected.

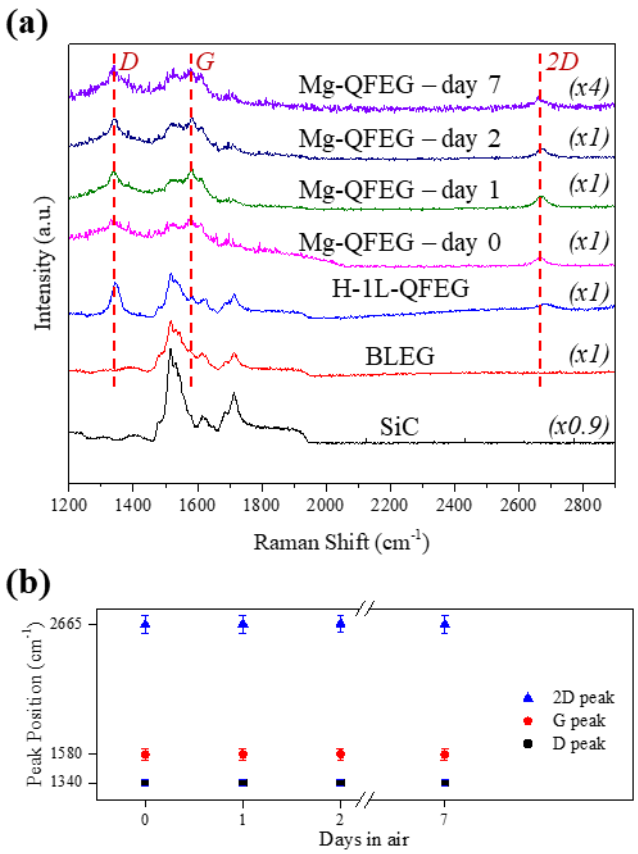

FIG. 5. (a) Raman spectra of Mg-1L-QFEG over 7 days in ambient air. The presence of the 2D peak indicates a decoupled graphene layer. (b) A lack of variation in the graphene peak positions suggest the charge remains invariant and the Mg intercalation is stable under ambient conditions.

However, EDS was unable to detect any significant amount of Mg or O near the SiC interface. This may be due to the lower amount of Mg intercalation with CVD compared to PVD, as suggested by XPS, such that the Mg is beneath the detection limit of EDS.

Direct measurement of the chemical stability of Mg-1L-QFEG using XPS or another surface analysis technique is challenging due to the presence of Mg particles on the surface as discussed previously. Attempts to remove the surface Mg through mechanical means or chemical etching resulted in damage to the underlying graphene. For that reason, we instead used Raman spectroscopy of graphene to identify changes in the charge or strain state of the graphene over time as indicated by shifts in the peak positions[43,44]. Raman spectra of Mg-1L-QFEG as a function of time after air exposure for up to 7 days are shown in Fig. 5a along with reference spectra for SiC, BLEG and H-1L-QFEG. As-grown BLEG has a Raman spectrum nearly identical to that of the SiC substrate. When the graphene buffer layer is decoupled from the SiC via hydrogen intercalation, passivation of the Si-terminated substrate surface breaks the covalent bonds restraining the graphene buffer layer and permits breathing mode vibrations such that the 2D peak appears, as seen in the example of H-1L-QFEG. Note that the post-intercalation presence of D and G peaks are also a result of the newly available graphene breathing modes as well. Intercalation of Mg to form Mg-1L-QFEG also produces the 2D peak which is an indication of successful intercalation. Fitting each individual Raman peak with a single Voigt curve, it was determined that there were no notable shifts in peak position over time for the 7-day duration investigated [Fig. 5b].

The extent of charge transfer and doping in graphene can be assessed via changes in the 2D peak position, with a shift toward lower wavenumber for electron doping[43]. The average 2D peak position for standard graphene is approximately 2700 cm^{-1}. While the 2D peak in as-grown

BLEG is nonexistent, H-1L-QFEG, reported as mildly p-doped[28], provides an adequate comparison to look for shifting of this peak position. Comparing the average 2D peak position of H-1L-QFEG samplings, 2703 ± 19 cm^{-1}, to the average for the Mg-1L-QFEG over 7 days, 2668 ± 3 cm^{-1}, the latter is redshifted by up to 30 cm^{-1}. The sub-2700 cm^{-1} value suggests an increase in electron doping relative to both the H-1LQFEG measured and the average value of standard graphene. This result is expected with the n-type doping effect expected based on prior studies of Mg intercalation[19,24]. Efforts were made to intercalate Mg into H-1L-QFEG as well. The results for the average 2D peak position of those samples, 2710 ± 15 cm^{-1}, are like that of H-1L-QFEG, indicating that there is minimal impact of the Mg on charge or strain of the graphene. It has been suggested that Mg will not intercalate into hydrogenated EG[19], so it is plausible these are equivalent results indicating a lack of Mg intercalation.

4.0 Conclusion

Evidence has been presented for CVD and PVD intercalation of Mg to form Mg-1L-QFEG and Mg-2L-QFEG, respectively. Spectroscopy, XPS, AR-XPS, and Raman, offer rapid techniques for determining successful intercalation and are reinforced by cross-section STEM-EDS micrographs of PVD synthesized Mg-2L-QFEG. Support for the stability of Mg-1L-QFEG in ambient conditions is suggested by an invariant 2D peak position in the Raman spectra over time. Thus, this suggests that graphene in Mg-1L-QFEG could be suitable for applications in ambient conditions. Moreover, Raman infers that there is strong electron doping of the graphene after Mg intercalation.

Both synthesis methods offer advantages and disadvantages. CVD allows for a cleaner and smoother graphene surface, and it allows for improved control of Mg exposure duration and concentration. Additionally, CVD allows for a broader range of intercalation conditions than PVD,

but this method is limited by the reduced flux of the Mg precursor which results in a lower yield of intercalated Mg. On the contrary, PVD allows for large gas phase concentrations of Mg over a short period of time at lower temperatures due to Mg's high vapor pressure. However, this results in increased surface roughness due to Mg particle formation on the EG surface. Furthermore, conditions for utilizing physical sources are restricted by their dependence on an outside heating source and how it integrates into the reactor configuration. The results demonstrate the viability of Mg intercalation via PVD and CVD that can be used to realize air-stable n-type graphene for device applications.

Acknowledgments

This material is based upon work supported by the National Science Foundation under the Graduate Research Fellowship Program (Grant No. DGE1255832) and DMR-1808900 and DMR-1905833. Part of the electron microscopy and spectroscopy analysis were supported by the Department of Energy under Grant No. DE-FG02-08ER46531. Any opinions, findings, and conclusions or recommendations expressed in this material are those of the author(s) and do not necessarily reflect the views of the National Science Foundation.

CRediT author statement

Patrick Rondomanski: Conceptualization, Methodology, Investigation, Validation, Formal Analysis, Writing- Original Draft **Anushka Bansal:** Investigation **Chengye Dong:** Resources **Ke Wang:** Investigation **Jennifer Gray:** Investigation **Jeffrey Shallenberger:** Investigation, Formal Analysis **Joshua Robinson:** Resources **Qi Li:** Supervision, Writing - Review and Editing,

Funding acquisition **Joan Redwing:** Supervision, Writing - Review and Editing, Funding acquisition

Conflicts of Interest

There are no conflicts of interest in this work.

References

1. Wang, R. *et al.* Graphene based functional devices: A short review. *Front. Phys.* **14**, 13603 (2018).
2. Liu, Z., Lau, S. P. & Yan, F. Functionalized graphene and other two-dimensional materials for photovoltaic devices: device design and processing. *Chem. Soc. Rev.* **44**, 5638–5679 (2015).
3. Singh, E., Meyyappan, M. & Nalwa, H. S. Flexible Graphene-Based Wearable Gas and Chemical Sensors. *ACS Appl. Mater. Interfaces* **9**, 34544–34586 (2017).
4. Papageorgiou, D. G., Kinloch, I. A. & Young, R. J. Mechanical properties of graphene and graphene-based nanocomposites. *Progress in Materials Science* **90**, 75–127 (2017).
5. Schwierz, F. Graphene Transistors: Status, Prospects, and Problems. *Proceedings of the IEEE* **101**, 1567–1584 (2013).
6. Rapid Detection of COVID-19 Causative Virus (SARS-CoV-2) in Human Nasopharyngeal Swab Specimens Using Field-Effect Transistor-Based Biosensor. https://pubs-acs-org.ezaccess.libraries.psu.edu/doi/epdf/10.1021/acsnano.0c02823 doi:10.1021/acsnano.0c02823.
7. Wei, J. *et al.* Enhanced performance of light-controlled conductive switching in hybrid cuprous oxide/reduced graphene oxide (Cu_2O/rGO) nanocomposites. *Opt. Lett., OL* **42**, 911–914 (2017).

8. Ding, Y. *et al.* Hollow Cu2O nanospheres loaded with MoS2/reduced graphene oxide nanosheets for ppb-level NO2 detection at room temperature. *J Hazard Mater* **416**, 126218 (2021).

9. Huang, X., Zeng, Z., Fan, Z., Liu, J. & Zhang, H. Graphene-Based Electrodes. *Advanced Materials* **24**, 5979–6004 (2012).

10. Chen, F. W., Ilatikhameneh, H., Klimeck, G., Chen, Z. & Rahman, R. Configurable Electrostatically Doped High Performance Bilayer Graphene Tunnel FET. *IEEE Journal of the Electron Devices Society* **4**, 124–128 (2016).

11. Szafranek, B. N., Fiori, G., Schall, D., Neumaier, D. & Kurz, H. Current Saturation and Voltage Gain in Bilayer Graphene Field Effect Transistors. *Nano Lett.* **12**, 1324–1328 (2012).

12. Efetov, D. K. & Kim, P. Controlling Electron-Phonon Interactions in Graphene at Ultrahigh Carrier Densities. *Phys. Rev. Lett.* **105**, 256805 (2010).

13. Wu, S. *et al.* Advances in two-dimensional heterostructures by mono-element intercalation underneath epitaxial graphene. *Progress in Surface Science* **96**, 100637 (2021).

14. Bonacum, J. P. *et al.* Atomic-resolution visualization and doping effects of complex structures in intercalated bilayer graphene. *Phys. Rev. Mater.* **3**, 064004 (2019).

15. Kwon, S.-J. *et al.* Extremely stable graphene electrodes doped with macromolecular acid. *Nat Commun* **9**, 2037 (2018).

16. Lv, R. *et al.* Nitrogen-doped graphene: beyond single substitution and enhanced molecular sensing. *Sci Rep* **2**, 586 (2012).

17. Bisti, F. *et al.* Electronic and geometric structure of graphene/SiC(0001) decoupled by lithium intercalation. *Phys. Rev. B* **91**, 245411 (2015).

18. Virojanadara, C., Zakharov, A. A., Watcharinyanon, S., Yakimova, R. & Johansson, L. I. A low-energy electron microscopy and x-ray photo-emission electron microscopy study of Li intercalated into graphene on SiC(0001). *New J. Phys.* **12**, 125015 (2010).

19. Kotsakidis, J. C. *et al.* Freestanding n-Doped Graphene via Intercalation of Calcium and Magnesium into the Buffer Layer–SiC(0001) Interface. *Chem. Mater.* **32**, 6464–6482 (2020).

20. Li, K. *et al.* Superconductivity in Ca-intercalated epitaxial graphene on silicon carbide. *Applied Physics Letters* **103**, 062601 (2013).

21. Sanders, S. *et al.* Engineering high charge transfer n-doping of graphene electrodes and its application to organic electronics. *Nanoscale* **7**, 13135–13142 (2015).

22. Han, K. S. *et al.* A non-destructive n-doping method for graphene with precise control of electronic properties via atomic layer deposition. *Nanoscale* **8**, 5000–5005 (2016).

23. Riedl, C., Coletti, C. & Starke, U. Structural and electronic properties of epitaxial graphene on SiC(0 0 0 1): a review of growth, characterization, transfer doping and hydrogen intercalation. *J. Phys. D: Appl. Phys.* **43**, 374009 (2010).

24. Grubišić-Čabo, A. *et al.* Magnesium-intercalated graphene on SiC: Highly n-doped air-stable bilayer graphene at extreme displacement fields. *Applied Surface Science* **541**, 148612 (2021).

25. Park, H. *et al.* Observation of Mg-induced structural and electronic properties of graphene. *Appl. Phys. Lett.* **109**, 193104 (2016).

26. Turker, F. *et al.* 2D Oxides Realized via Confinement Heteroepitaxy. *Advanced Functional Materials* **33**, 2210404 (2023).

27. Briggs, N. *et al.* Atomically thin half-van der Waals metals enabled by confinement heteroepitaxy. *Nat. Mater.* **19**, 637-+ (2020).

28. Briggs, N. *et al.* Epitaxial graphene/silicon carbide intercalation: a minireview on graphene modulation and unique 2D materials. *Nanoscale* **11**, 15440–15447 (2019).

29. Pham, V. D., Dong, C. & Robinson, J. A. Atomic structures and interfacial engineering of ultrathin indium intercalated between graphene and SiC substrate. *Nanoscale Adv.* 10.1039.D3NA00630A (2023) doi:10.1039/D3NA00630A.

30. Bansal, A. *et al.* Toward a Mechanistic Understanding of the Formation of 2D-GaNX in Epitaxial Graphene. *ACS Nano* **17**, 230–239 (2023).

31. Al Balushi, Z. Y. *et al.* Two-dimensional gallium nitride realized via graphene encapsulation. *Nature Mater* **15**, 1166–1171 (2016).

32. Robinson, J. *et al.* Nucleation of Epitaxial Graphene on SiC(0001). *ACS Nano* **4**, 153–158 (2010).

33. de Heer, W. A. *et al.* Epitaxial graphene. *Solid State Communications* **143**, 92–100 (2007).

34. Koleske, D. *et al.* Issues associated with the metalorganic chemical vapor deposition of ScGaN and YGaN alloys. (2023) doi:10.2172/961650.

35. Mierry, P. de *et al.* Influence of the Mg precursor on the incorporation of Mg in MOVPE grown GaN. *Materials Research Society Internet Journal of Nitride Semiconductor Research* **5**, e8 (2000).

36. Liu, F., Wang, M., Chen, Y. & Gao, J. Thermal stability of graphene in inert atmosphere at high temperature. *Journal of Solid State Chemistry* **276**, 100–103 (2019).

37. De Jong, T. A. *et al.* Intrinsic stacking domains in graphene on silicon carbide: A pathway for intercalation. *Phys. Rev. Materials* **2**, 104005 (2018).

38. Kotsakidis, J. C. *et al.* Increasing the Rate of Magnesium Intercalation Underneath Epitaxial Graphene on 6H-SiC(0001). *Adv Materials Inter* **8**, 2101598 (2021).

39. Riedl, C. Epitaxial Graphene on Silicon Carbide Surfaces: Growth, Characterization, Doping and Hydrogen Intercalation. (Friedrich-Alexander-Universität Erlangen-Nürnberg, 2010).

40. Riedl, C., Coletti, C., Iwasaki, T., Zakharov, A. A. & Starke, U. Quasi-Free-Standing Epitaxial Graphene on SiC Obtained by Hydrogen Intercalation. *Phys. Rev. Lett.* **103**, 246804 (2009).

41. Ostler, M. *et al.* Decoupling the Graphene Buffer Layer from SiC(0001) via Interface Oxidation. *MSF* **717–720**, 649–652 (2012).

42. Data retrieved from the Materials Project for Mg2Si (mp-1367) from database version v2022.10.28. *Materials Project* https://next-gen.materialsproject.org/materials/mp-1367?chemsys=Mg-Si.

43. Casiraghi, C., Pisana, S., Novoselov, K. S., Geim, A. K. & Ferrari, A. C. Raman fingerprint of charged impurities in graphene. *Appl. Phys. Lett.* **91**, 233108 (2007).

44. Robinson, J. A. *et al.* Raman Topography and Strain Uniformity of Large-Area Epitaxial Graphene. *Nano Lett.* **9**, 964–968 (2009).